

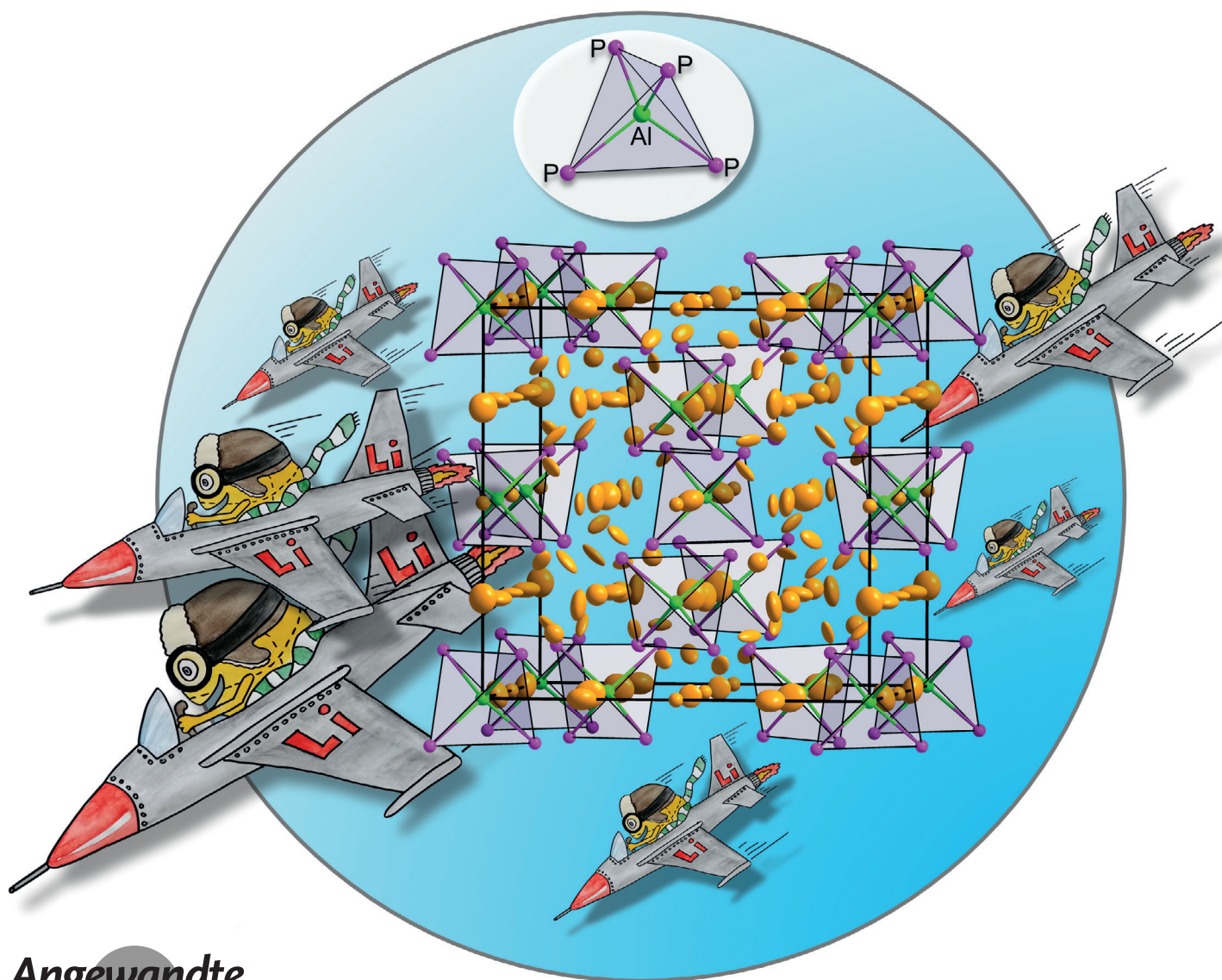
VIP Solid Electrolytes Very Important Paper

International Edition: DOI: 10.1002/anie.201914613  
German Edition: DOI: 10.1002/ange.201914613

# Fast Lithium Ion Conduction in Lithium Phosphidoaluminates

Tassilo M. F. Restle, Christian Sedlmeier, Holger Kirchhain, Wilhelm Klein, Gabriele Raudaschl-Sieber, Volker L. Deringer, Leo van Wüllen, Hubert A. Gasteiger, and Thomas F. Fässler\*

Dedicated to Professor Hubert Schmidbaur on the occasion of his 85th birthday



**Abstract:** Solid electrolyte materials are crucial for the development of high-energy-density all-solid-state batteries (ASSB) using a nonflammable electrolyte. In order to retain a low lithium-ion transfer resistance, fast lithium ion conducting solid electrolytes are required. We report on the novel superionic conductor  $\text{Li}_9\text{AlP}_4$  which is easily synthesised from the elements via ball-milling and subsequent annealing at moderate temperatures and which is characterized by single-crystal and powder X-ray diffraction. This representative of the novel compound class of lithium phosphidoaluminates has, as an undoped material, a remarkable fast ionic conductivity of  $3 \text{ mScm}^{-1}$  and a low activation energy of  $29 \text{ kJ mol}^{-1}$  as determined by impedance spectroscopy. Temperature-dependent  $^7\text{Li}$  NMR spectroscopy supports the fast lithium motion. In addition,  $\text{Li}_9\text{AlP}_4$  combines a very high lithium content with a very low theoretical density of  $1.703 \text{ g cm}^{-3}$ . The distribution of the Li atoms over the diverse crystallographic positions between the  $[\text{AlP}_4]^{9-}$  tetrahedra is analyzed by means of DFT calculations.

## Introduction


The development of advanced energy-storage technologies plays a key role in realizing electric vehicles.<sup>[1–4]</sup> Next-generation high-energy-density storage systems require low flammability, good electrochemical stability, and fast charging times. Li-ion batteries based on organic electrolytes hinder the commercialization of long-range electric vehicles. All-solid-state batteries (ASSBs) are promising candidates to overcome safety concerns of currently used Li-ion batteries with flammable organic liquid electrolytes.<sup>[5–8]</sup> Replacing the organic liquid electrolyte by an inorganic solid-state electrolyte (SSE), ASSBs offer high energy and power density, mechanical stability, and safety benefits.<sup>[9–14]</sup> However, ASSBs are limited by the slow ionic mobility of the SSE.<sup>[15]</sup> Hence, the discovery, characterization, and optimization of lithium superionic conducting solid phases are among the main


aspects of today's battery material research.<sup>[8,16–18]</sup> Despite the clear advantage of ASSBs, achieving Li-ion conductivity in SSEs comparable to that in liquid electrolytes ( $> 10 \text{ mScm}^{-1}$ ) is a demanding task.<sup>[9]</sup> In the last decades, different crystalline materials have been proven to act as lithium conductors such as perovskite-type structures,<sup>[19–22]</sup> lithium superionic conductor (LISICON)-type structures,<sup>[23–26]</sup> thio-LISICON-type structures and thiophosphates,<sup>[27–32]</sup> sodium superionic conductor (NASICON)-type structures,<sup>[33,34]</sup> garnet-type structures,<sup>[35–37]</sup> lithium argyrodites,<sup>[38]</sup> lithium borohydrides,<sup>[39]</sup> lithium nitrides,<sup>[40–42]</sup> lithium hydrides,<sup>[43]</sup> and lithium halides.<sup>[44]</sup> The best lithium ion conductors currently known are rather complex systems such as  $\text{Li}_{9.54}\text{Si}_{1.74}\text{P}_{1.44}\text{S}_{11.7}\text{Cl}_{0.3}$  and  $\text{Li}_{6+x}\text{M}_3\text{Sb}_{1-x}\text{S}_5\text{I}$  ( $\text{M} = \text{Si}, \text{Ge}, \text{Sn}$ ) with an ionic conductivity of 25 and  $24 \text{ mScm}^{-1}$ , respectively, outperforming the conductivity of liquid-based electrolytes.<sup>[45,46]</sup> By increasing the carrier densities, changing the diffusion pathways of the mobile species, creating vacancies or increasing structural defects, the ionic conductivity can be further optimized.<sup>[8,16]</sup> An effective way to increase the carrier density is especially the aliovalent substitution of cations: for example, in  $\text{Li}_3\text{PS}_4$  making a formal substitution of “ $\text{P}^{5+}$ ” with “ $\text{Ge}^{4+}$ ” results in  $\text{Li}_{3.25}\text{Ge}_{0.25}\text{P}_{0.75}\text{S}_4$  having a four times higher ionic conductivity.<sup>[28]</sup>

On the way to new candidates with good lithium ion conducting abilities, we recently have investigated lithium phosphidosilicates and phosphidogermanates.<sup>[47,48]</sup> The idea of replacing  $\text{S}^{2-}$  by  $\text{P}^{3-}$  enables the accommodation of even more lithium ions in the structures. Since our first report in 2016 on the aristo-type  $\text{Li}_8\text{SiP}_4$ ,<sup>[47]</sup> also  $\text{Li}_4\text{SiP}_6$  was established as good lithium ion conductor.<sup>[49]</sup> Recently, we have also shown that the system can be extended to the heavier homologue germanium and that for  $\text{Li}_8\text{GeP}_4$  two Li-ion conducting modifications exist which display ionic conductivities of up to  $8.6 \times 10^{-5} \text{ Scm}^{-1}$  at 298 K.<sup>[48]</sup> Structurally, phosphidosilicates and phosphidogermanates are built up by  $[\text{TiP}_4]^{8-}$  tetrahedra, where  $\text{Ti}$  denotes the respective tetrel atom (Si, Ge). Relating to the building principles of oxidosilicates, thiosilicates, and thiophosphates, these tetra-

[\*] T. M. F. Restle, W. Klein, T. F. Fässler  
Department of Chemistry  
Chair for Inorganic Chemistry with Focus on New Materials  
Technische Universität München  
Lichtenbergstraße 4, 85747 Garching (Germany)  
E-mail: Thomas.Faessler@lrz.tum.de  
C. Sedlmeier, H. A. Gasteiger  
Department of Chemistry and Catalysis Research Center  
Chair of Technical Electrochemistry  
Technische Universität München  
Lichtenbergstraße 4, 85747 Garching (Germany)  
G. Raudaschl-Sieber  
Department of Chemistry  
Chair of Inorganic and Metal-Organic Chemistry  
Technische Universität München  
Lichtenbergstraße 4, 85747 Garching (Germany)  
H. Kirchhain, L. van Wüllen  
Department of Physics, University of Augsburg  
Universitätsstraße 1, 86159 Augsburg (Germany)

V. L. Deringer  
Department of Engineering, University of Cambridge  
Cambridge CB2 1PZ (UK)  
V. L. Deringer  
Present address: Department of Chemistry, University of Oxford  
Oxford OX1 3QR (UK)

 Supporting information (including details of the crystal structure determination, coordination polyhedra, EDX measurements, experimental powder X-ray diffraction pattern, figure of the ternary phase system Li-Al-P, impedance measurement procedure, computational details, and additional computational data) and the ORCID identification number(s) for the author(s) of this article can be found under:  
<https://doi.org/10.1002/anie.201914613>.

 © 2019 The Authors. Published by Wiley-VCH Verlag GmbH & Co. KGaA. This is an open access article under the terms of the Creative Commons Attribution License, which permits use, distribution and reproduction in any medium, provided the original work is properly cited.

hedra can be formally condensed and covalently connected by sharing edges or corners; hence a large variety of structure motifs can be gained. The idea of phosphide-based structures as ionic conductors results from the aliovalent substitution of  $[TiS_4]^{4-}$  tetrahedra, which are a key building block in sulfide-based electrolytes, leading to the analogous complex anions based on phosphorus. Due to the resulting higher charge,  $[TiP_4]^{8-}$  tetrahedra allow for more lithium ions per formula unit for charge compensation when compared to  $[TiS_4]^{4-}$ . In addition, the more negatively charged  $P^{3-}$  is more polarizable than  $S^{2-}$ .

The coincidence of a higher charge carrier density due to more Li ions for charge compensation together with a large number of vacancies is considered as an important prerequisite for a higher lithium ion conductivity. Certainly, this aspect must be in line with a low activation energy for lithium mobility as it occurs in structures with an effective polyhedral connectivity.<sup>[50]</sup> An aliovalent substitution of formal “ $Si^{4+}$ ” by “ $Al^{3+}$ ” and formation of  $[AlP_4]^{9-}$  instead of  $[SiP_4]^{8-}$  tetrahedra allow for the presence of an even higher number of lithium ions and a strong influence on the Li occupation in voids. Ternary phases comprising the elements lithium, aluminum, and phosphorus were scarcely investigated. In the 1950s Juza et al. reported briefly the first lithium phosphidoaluminate,  $Li_3AlP_2$ , and described its structure as a strongly distorted fluorite-type lattice in which P atoms form a close-packed atom arrangement and Al and Li atoms are randomly distributed over the tetrahedral sites.<sup>[51]</sup> Occupation of Li ions in octahedral sites was, however, not considered. Two further publications on  $Li_3AlP_2$  were based on the poor structural characterization.<sup>[52,53]</sup>

Here we report on the lithium-richest representative of the phosphidoaluminates, obtained by formal aliovalent substitution of “ $Ti^{4+}$ ” by “ $Al^{3+}$ ” in  $Li_8TiP_4$ . The insertion of  $Al^{3+}$  leads to formally ninefold negatively charged  $[AlP_4]^{9-}$  tetrahedra, resulting in an even higher lithium density per formula unit and a change in the spatial extent of the diffusion pathways. Due to the nature of the structure in which P atoms form a cubic-close-packing arrangement, there are still a high number of unoccupied octahedral sites present. We expect that an increase of the carrier density will also lead to an increase of the ionic conductivity. Indeed, only recently, ab initio simulations suggested that doping of the moderate lithium-ion conductor  $Li_2SiP_2$  with Al could enhance the ionic conductivity.<sup>[47,54]</sup>

## Results and Discussion

### Synthesis and Crystal Structure of $Li_9AlP_4$

$Li_9AlP_4$  was synthesized from the elements by a two-step procedure. After ball-milling of stoichiometric amounts of Li, Al and P, the powder mixture was annealed at 973 K for one day yielding almost phase-pure  $Li_9AlP_4$  with 2.3(1) wt % LiP impurities (see Figure 1). Complete data of the Rietveld refinement are given in the Supporting Information (Tables S1 and S2). Single crystals of  $Li_9AlP_4$  were obtained by the direct reaction of the elements at 1073 K with a slight

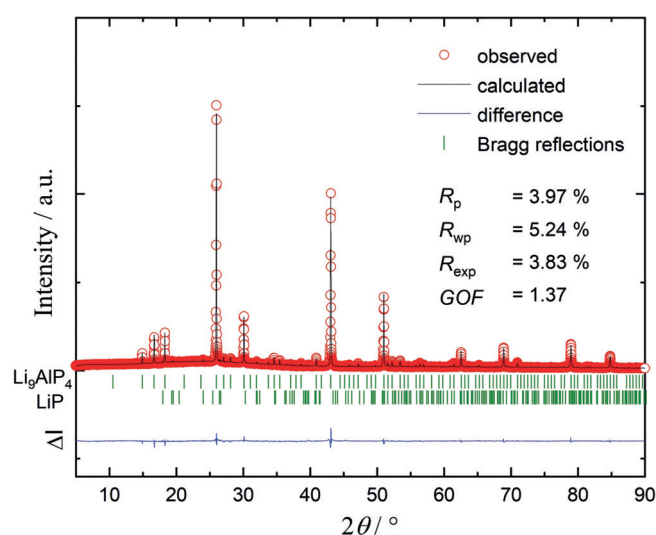


**Figure 1.** Rietveld analysis of the powder X-ray diffractogram of  $Li_9AlP_4$ . The red dots indicate the observed intensities, the black line the calculated intensities, and the blue line the difference between both. Bragg positions are marked by green dashes.

excess of P using a ratio of 9:1:4.2 (Li:Al:P). The resulting product contains besides  $Li_9AlP_4$  also  $Li_3P$  and  $TaP$  (see Figure S4). Energy-dispersive X-ray spectroscopy (EDX) investigations of single crystals show an Al/P ratio which is in very good agreement with the expected values (see Table S6).  $Li_9AlP_4$  can also be synthesized starting from  $Li_3P$ . However, again unreacted  $Li_3P$  remains as a contamination (see Figure S5). According to EDX measurements, the single crystals were free of Ta. The details of the structure refinement of the single-crystal X-ray diffraction of  $Li_9AlP_4$  are listed in Table 1 (further data are given in Tables S3 and S4 in the Supporting Information).

According to single-crystal and powder X-ray structure determination and refinement,  $Li_9AlP_4$  crystallizes in the cubic space group  $P\bar{4}3n$  (no. 218). The structure of  $Li_9AlP_4$  is built up of isolated  $[AlP_4]^{9-}$  tetrahedra surrounded by  $Li^+$  ions (Figure 2a). The  $AlP_4$  tetrahedra are slightly distorted with P-Al-P angles ranging from  $110.89(2)^\circ$  to  $108.77(2)^\circ$  in comparison to the ideal tetrahedron angle of  $109.74^\circ$ . The Al-P bonds at 2.425(1) and 2.433(1) Å are longer than the Al-P bonds observed in compounds with connected  $AlP_4$  tetrahedra like  $AlP$  (2.360(1) Å),  $Na_3AlP_2$  (2.376(4) Å), and  $Sr_3Al_2P_4$  (2.377(3) Å–2.417(2) Å).<sup>[55–57]</sup>

For the discussion of the coordination polyhedra of Li atoms, the structure is considered as a distorted cubic-face-centered packing of P atoms with Li and Al atoms filling voids in between and Wyckoff positions giving the multiplicity of the site. With  $Z=8$ , there are 32 P atoms per unit cell resulting in 64 tetrahedral and 32 octahedral voids. The atoms Al1 and Al2 occupy 1/8 of the tetrahedral voids on Wyckoff positions 2a and 6d, respectively. We like to point out that the Al atoms are fully ordered, and no mixed occupancy of Al and Li occurs, in contrast to the mixed Li/Si occupancy in the Li-rich phase  $Li_{14}SiP_6$ .<sup>[49]</sup> The remaining tetrahedral voids in the title compound are occupied by Li atoms as follows: Li1, Li4, and Li5 (on Wyckoff positions 6b, 12f, and 24i, respectively)

**Table 1:** Crystallographic data and refinement parameters of the SC-XRD analysis of  $\text{Li}_9\text{AlP}_4$ .

Empirical formula	$\text{Li}_{8.7(2)}\text{AlP}_4$
Formula weight [ $\text{g mol}^{-1}$ ]	210.93
Crystal size [ $\text{mm}^3$ ]	$0.2 \times 0.2 \times 0.1$
Crystal color	dark brown-golden
Crystal shape	plate
$T$ [K]	150(1)
Space group	$P\bar{4}3n$ (no. 218)
Unit cell dimension [ $\text{\AA}$ ]	$a = 11.852(1)$
$V$ [ $\text{\AA}^3$ ]	1664.7(6)
$Z$	8
$\rho$ (calc.) [ $\text{g cm}^{-3}$ ]	1.703
$\mu$ [ $\text{mm}^{-1}$ ]	0.908
$\theta$ Range [ $^\circ$ ]	2.430–32.494
Index range $hkl$	$-17 \leq h \leq 17$ $-17 \leq k \leq 16$ $-17 \leq l \leq 12$
Reflections collected	13 214
Independent reflections	1013
$R_{\text{int}}$	0.0498
Reflections with $I > 2\sigma(I)$	758
Data/restraints/parameter	1013/0/63
Absorption correction	empirical
Goodness-of-fit on $F^2$	1.277
Final $R$ indices [ $I > 2\sigma(I)$ ] <sup>[a,b]</sup>	$R_1 = 0.026$ $wR_2 = 0.067$
$R$ indices (all data) <sup>[a,b]</sup>	$R_1 = 0.041$ $wR_2 = 0.080$
Largest diff. peak and hole [ $\text{e}\text{\AA}^{-3}$ ]	0.362/−0.417
Depository no.	CSD-1962473

$$[a] R_1 = \frac{\sum ||F_o| - |F_c||}{\sum |F_o|}$$

$$[b] wR_2 = \frac{[\sum w(F_o^2 - F_c^2)^2]}{[\sum w(F_o^2)^2]}^{1/2}$$

are fully occupied, whereas Li2 and Li3 (on Wyckoff positions 6c and 8e, respectively) are partially occupied with site occupation factors 0.50(5) and 0.71(4), respectively, based on single-crystal structure determination data. Hence, the overall occupation of tetrahedral positions by lithium is 91 %.

The occupation of the 32 larger octahedral voids reveals two interesting aspects. The voids are partially occupied and in addition, we see for the first time that the Li atoms are not necessarily located at the center of the  $\text{P}_6$  octahedra (Figure 2c). The 32 octahedral voids can be distinguished by two crystallographically different Wyckoff positions that are both partially occupied with Li: Li7 on Wyckoff position 8e with site occupation factor (*sof*) 0.25(4) and a split position of Li6a and Li6b on Wyckoff position 24i with *sof* 0.46(2) and *sof* 0.23(2), respectively (Figure 2b). The overall occupation of the octahedral voids, therefore, is 58 %.

Due to the good quality of the crystallographic data it becomes obvious that Li6a, Li6b, and Li7 are not located in the centers of the octahedra, and the data also allow the determination of split positions in one octahedral void as anticipated for other lithium ion conducting materials that have Li ions in octahedral environments, as in garnets ( $\text{Li}_7\text{La}_3\text{Zr}_2\text{O}_{12}$ ) and sulfide-based materials ( $\text{Li}_{10}\text{GeP}_2\text{S}_{12}$ ).<sup>[58,59]</sup> The refined positions of the octahedrally coordinated Li ions are shifted towards the triangular faces of the octahedra, where the face-sharing  $\text{LiP}_4$  tetrahedra of the partially occupied Li sites Li2 and Li3 are located.

All Li atoms exhibit large displacement ellipsoids (Figure 2a) which points towards a static or thermal displacement indicative of a high lithium ion mobility. All atomic positions except Li1 were refined anisotropically. Interestingly, the octahedral positions Li6a and Li6b exhibit ellipsoids that point towards the center of the triangular faces of the neighboring tetrahedral voids that are only partially filled with Li2 and Li3 (Figure 2b).

The high structural diversity of the Li atoms including disorder and split positions reflects the possibility of high lithium ion mobility. Li–P distances in the tetrahedral voids range from 2.50(1) to 2.73(1)  $\text{\AA}$ , and in the octahedral voids they range from 2.56(1) to 3.46(1)  $\text{\AA}$ . The bond lengths are similar to those in other ternary phases containing Li and P, such as  $\text{Li}_8\text{SiP}_4$ ,  $\text{Li}_2\text{SiP}_2$ ,  $\text{Li}_{10}\text{SiP}_2$ , and  $\text{Li}_3\text{Si}_3\text{P}_7$ .<sup>[47,60]</sup>

According to the valence rules,  $\text{Li}_9\text{AlP}_4$  is an electron-precise compound and can be described as  $(\text{Li}^+)_9[\text{AlP}_4]^{9-}$ , with formally two negative charges for the P atoms and one negative charge for the Al atom, balanced by nine  $\text{Li}^+$  ions.

### DFT Calculations

DFT computations based on the experimentally derived structural information were performed to serve a double purpose: first, to corroborate the refined structural model obtained from experiments; second, to obtain information about stability trends and the coordination of individual atoms in the presence of crystallographic disorder. We constructed a series of discrete atomistic models which approximate the disordered structure (making simplifications as detailed in the Supporting Information). The energetic stability of the new compound as compared to competing phases is analyzed according to the line in the ternary composition (Gibbs) diagram. Since  $\text{Li}_9\text{AlP}_4$  is located on the line between the binaries  $\text{Li}_3\text{P}$  and  $\text{AlP}$  (Figure S6), it is straightforward to inquire the formation energy according to  $3\text{Li}_3\text{P} + \text{AlP} (= \text{Li}_9\text{AlP}_4)$  and to assess whether the title compound is stable with regard to the constituent binaries. The computed energies of ten randomized structural models were compared to those of the competing binary phases ( $3\text{Li}_3\text{P} + \text{AlP}$ ) which are set as energy zero. The formation of the ternary title compound from the binaries is energetically favored by approximately  $30 \text{ kJ mol}^{-1}$  (Figure 3a and the Supporting Information), even without taking configurational entropy into account (which will further stabilize the ternary phase, as there are no partially occupied crystallographic positions in either  $\text{Li}_3\text{P}$  or  $\text{AlP}$ ).

In addition to the energetic stability, having an ensemble of computationally optimized structural models allows us to quantify the distribution of interatomic distances and to compare with experimental results. Smoothed histograms over all ten structures are given in Figure 3b. The computed Al–P distances in the relaxed structures are 2.44(4)  $\text{\AA}$ , with a narrow distribution indicating the rigidity of the tetrahedral  $\text{AlP}_4$  units. The Li–P distributions peak at 2.6  $\text{\AA}$ , but include a substantial amount of larger distances, reflecting the more disordered nature of the Li atoms which are often shifted away from the centers of the octahedral voids. The distribu-

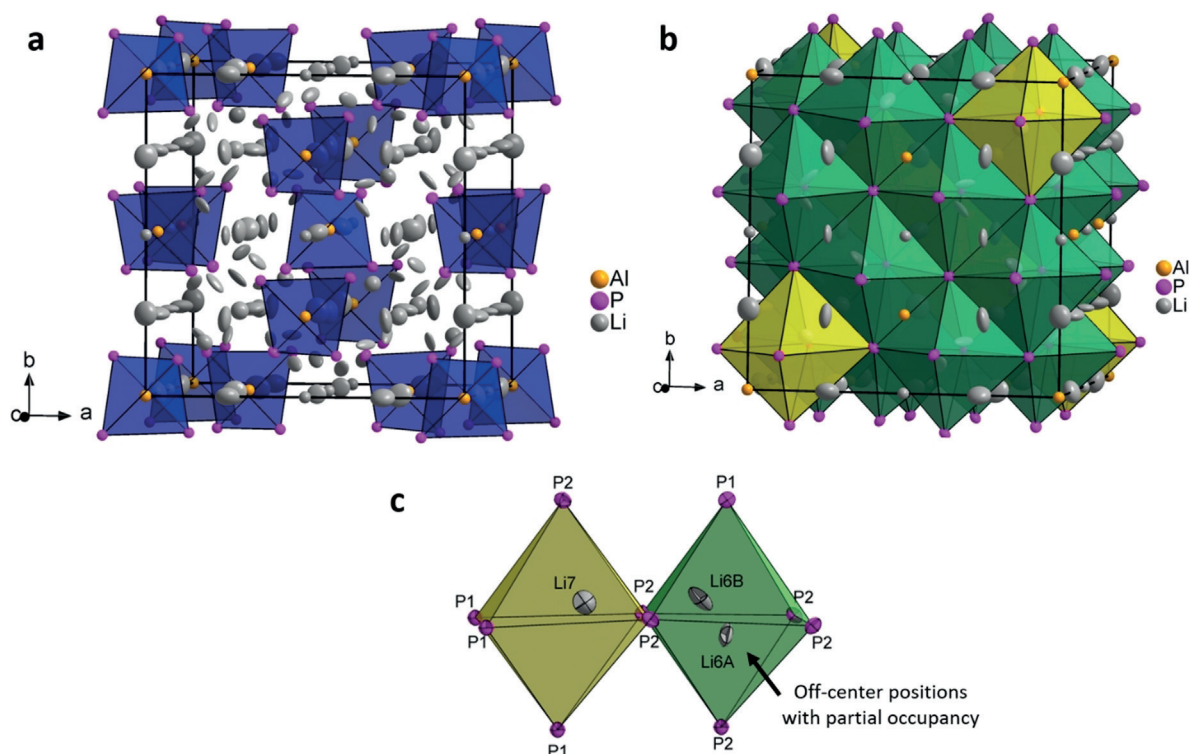


**Figure 2.** The crystal structure of  $\text{Li}_9\text{AlP}_4$  as determined from experimental data. a) Unit cell of  $\text{Li}_9\text{AlP}_4$ . The  $[\text{AlP}_4]^{9-}$  tetrahedra are highlighted in blue.  $\text{Li}^+$  ions are located in tetrahedral and octahedral voids; some of them exhibit partial occupations (Table S3). b) Unit cell with emphasis on the two crystallographically independent octahedral voids: polyhedra of  $\text{Li6a/Li6b}$  and  $\text{Li7}$  are shown in green and yellow, respectively. c) Closeup of neighboring octahedral voids with partially occupied  $\text{Li6a}$ ,  $\text{Li6b}$ , and  $\text{Li7}$  positions. Li, Al, and P are depicted in gray, orange, and purple, respectively (displacement ellipsoids set at 90% probability at 150 K).

tion of  $\text{Li}\cdots\text{Li}$  distances in the relaxed structures spans a broad range, starting at  $\approx 2.4$  Å, peaking at  $\approx 2.6$  Å, and becoming significantly less pronounced beyond 3.0 Å, in good agreement with the experimental observations (Table S5).

### Impedance Spectroscopy

The lithium ion conductivity of  $\text{Li}_9\text{AlP}_4$  was determined from impedance measurements in a blocking electrode configuration. Impedance spectra at different temperatures (273, 298, 313, 333, and 353 K according to the temperature profile shown in the inset) are displayed in Figure 4a and feature a semicircle at high frequencies and a low-frequency tail. The semicircle can be described as parallel circuit element of a resistor and a constant phase element ( $R/Q$ ), with  $R$  representing both intragrain and grain boundary contributions to the lithium ion transport which could not be resolved, and thus only the total ionic resistance of the sample could be determined. For the constant phase element, the fit of the data acquired at 298 K resulted in  $\alpha$  values of  $\approx 0.87$  and  $Q$  parameters with a value of  $\approx 17 \times 10^{-9} \text{ F s}^{(\alpha-1)}$ ; the ionic conductivity was determined to be  $\sigma_{\text{Li}}(\text{Li}_9\text{AlP}_4) = (3.03 \pm 0.16) \times 10^{-3} \text{ S cm}^{-1}$  at 298 K (obtained from three independently measured cells). The activation energy for lithium ion transport (Figure 4b) was investigated by temperature-de-

pendent impedance measurements in the range from 273–353 K, yielding  $E_{\text{A}}^{\text{PEIS}}$  of  $28.5 \pm 0.8 \text{ kJ mol}^{-1}$  ( $\approx 0.29 \text{ eV}$ ); this was determined from three independently measured cells, using the  $\sigma_{\text{Li}}T$  values of only the first heating and cooling cycle of each sample. This activation energy is in very good agreement with the value obtained by NMR spectroscopy (shown below). The temperature ramp of a heating and cooling cycle is displayed in the inset of Figure 4a. Colored dots indicate at which temperatures PEIS measurements were performed. In this context it should be mentioned that conductivities (and thus the product  $\sigma_{\text{Li}}T$ ) for heating and cooling differ by less than 6%. Error bars are calculated separately for heating and cooling steps by taking the mean of three independent measurements obtained from three cells. DC polarization measurements in the range from 50–150 mV reveal an electronic conductivity of  $(2.0 \pm 0.8) \times 10^{-7} \text{ S cm}^{-1}$  at 298 K (based on the standard deviation of two cells).

### $^6\text{Li}$ and $^7\text{Li}$ NMR Spectroscopy

The  $^6\text{Li}$  MAS NMR spectrum at room temperature shows one signal at a chemical shift of 4.19 ppm (Figure 5). The fitting of a generalized Lorentzian function to the experimental data proves the presence of only one signal as observed before for related compounds.<sup>[47,48]</sup> Since the shifts

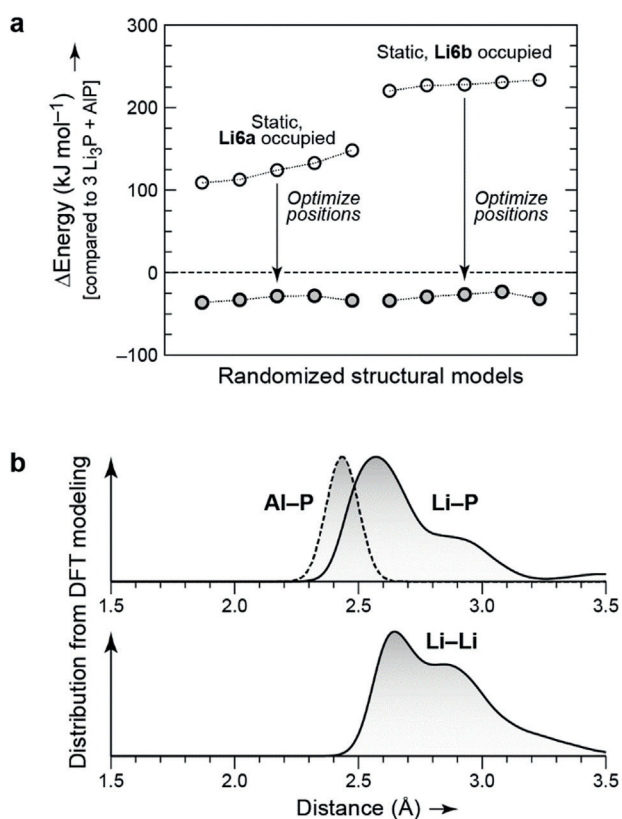


**Figure 3.** a) DFT-computed energy of 10 randomized structural models, compared to that of the competing binary phases ( $3\text{Li}_3\text{P} + \text{AlP}$ ) which are set as energy zero. The models are ordered by ascending (unrelaxed) energy; lines connecting symbols are only guides to the eye. Static computations (using the experimental structure; open circles) indicate a clear preference for the Li6a over the Li6b site. DFT optimization of these structures (arrows) yields an ensemble of models that are all more favorable than the competing binaries and are essentially degenerate in energy (see the Supporting Information for further details). b) Distribution of interatomic distances in randomized structural models of  $\text{Li}_9\text{AlP}_4$ , optimized using DFT, as detailed in the Supporting Information. Kernel density estimates (“smoothed histograms”) with a bandwidth of  $0.05\text{ \AA}$  are shown to characterize all relevant contacts collected over 10 structural models, which approximate the real structure within the limits of theory.

of Li atoms in tetrahedral and octahedral voids are not distinguishable, it can be assumed that all lithium ions are mobile at room temperature.

Static  $^7\text{Li}$  NMR spectra were recorded as a function of temperature to study the dynamic behavior of the lithium ions. The central transition of the  $I=3/2$  nucleus  $^7\text{Li}$  experiences a broadening only from the homo- ( $^7\text{Li}-^7\text{Li}$ ) and heteronuclear (here:  $^7\text{Li}-^{31}\text{P}$ ) dipolar couplings. Since both types of interactions scale with the second Legendrian ( $3\cos^2\beta-1$ ), any dynamic process should produce a (partial) averaging of the orientational dependence and hence entail a narrowing of the NMR signal.

At 290 K, the static  $^7\text{Li}$  spectrum (Figure 6a top) displays a homogeneous Lorentzian shape with a linewidth of 640 Hz. Upon cooling, the signal gradually broadens, developing a Gaussian line shape with a linewidth of 10.1 kHz (Figure 6a bottom). At intermediate temperatures (166 K and 200 K),

the line shape indicates some heterogeneity, which may be related to a distribution of activation energies for the Li ions occupying eight distinct crystallographic positions. Individual contributions from the different Li sites in the crystal lattice could not be resolved. For temperatures  $> 234\text{ K}$  a homogeneous line shape is observed, indicating all Li ions are mobile.

The temperature-dependent evolution of the linewidth (FWHH; full width at half height) of the  $^7\text{Li}$  NMR signal is shown in Figure 6b. A rough estimation of the activation energy of lithium motion is possible employing the empirical Waugh–Fedin relation  $E_A$  ( $\text{kJ mol}^{-1}$ ) =  $0.156 T_{\text{onset}}$  (K).<sup>[61]</sup> As the onset temperature, we identified the temperature at which the linewidth is given by  $(\nu_{\text{rigid lattice}} - \nu_{\text{mot. narrowing}})/2$ . This leads to an approximate onset temperature of 160 K which translates to an activation energy of  $25\text{ kJ mol}^{-1}$ .

## Conclusion

Recently, we reported the synthesis and characterization of  $\text{Li}_{14}\text{SiP}_6$ , for which we had optimized the ionic conductivity ( $\approx 1\text{ mS cm}^{-1}$ ) in lithium phosphidotetrelates by increasing the amount of lithium compared to  $\text{Li}_8\text{SiP}_4$ .<sup>[49]</sup> With  $\text{Li}_9\text{AlP}_4$  we now show that these materials can be further optimized, namely by full aliovalent replacement of the tetrelate atom. Compared to the ionic conductivities in  $\text{Li}_8\text{SiP}_4$  ( $4.5 \times 10^{-5}\text{ S cm}^{-1}$ ) and  $\alpha/\beta\text{-Li}_8\text{GeP}_4$  ( $1.8 \times 10^{-5}\text{ S cm}^{-1}$ ,  $8.6 \times 10^{-5}\text{ S cm}^{-1}$ ), via aliovalent substitution by aluminum and the associated higher lithium content in the structure alongside with a change in the distribution of vacancies (Table 2), the conductivity in  $\text{Li}_9\text{AlP}_4$  is strongly increased up to  $3.0(2)\text{ mS cm}^{-1}$  at room temperature. Concomitantly, the activation energy determined by impedance measurements drops significantly from 42 ( $\alpha\text{-Li}_8\text{GeP}_4$ ), 39 ( $\text{Li}_8\text{SiP}_4$ ), and  $38\text{ kJ mol}^{-1}$  ( $\beta\text{-Li}_8\text{GeP}_4$ ) to  $29\text{ kJ mol}^{-1}$  in  $\text{Li}_9\text{AlP}_4$ .

$\text{Li}_9\text{AlP}_4$  is easily accessible via ball-milling and crystallizes in the cubic space group  $P\bar{4}3n$  (no. 218). First-principles computations suggest that  $\text{Li}_9\text{AlP}_4$  is approximately  $30\text{ kJ mol}^{-1}$  more stable than the constituent binary phosphides. The structure of  $\text{Li}_9\text{AlP}_4$  shows a close relationship to the recently characterized lithium ion conductors  $\text{Li}_8\text{SiP}_4$ ,  $\alpha\text{-Li}_8\text{GeP}_4$ , and  $\beta\text{-Li}_8\text{GeP}_4$ . However, in  $\text{Li}_9\text{AlP}_4$  the highly negatively charged, isolated  $[\text{AlP}_4]^{9-}$  tetrahedra make it possible to accommodate a higher number of lithium ions per formula unit than in the phosphidotetrelates and therefore the new compound shows a much better Li ion conductivity. Whereas  $\text{Li}_8\text{GeP}_4$  adopts both the  $\alpha$  modification (space group  $Pa\bar{3}$ , no. 205) at lower temperature and the  $\beta$  modification at higher temperatures (space group  $P\bar{4}3n$ , no. 218),  $\text{Li}_9\text{AlP}_4$  crystallizes exclusively in analogy to the  $\beta$  modification. These phosphidosilicates, -germanates, and -aluminates can be described as a close packing of P atoms with four octahedral and eight tetrahedral voids per formula unit. Consequently, Al, Si, and Ge atoms occupy 1/8 of the tetrahedral voids forming covalently connected Al–P, Si–P, and Ge–P bonds, respectively, and are located on fixed fully occupied positions in the structure. The series of compounds now give insight into the occupancy of the lithium atoms which varies according to Table 2. By comparing the lithium

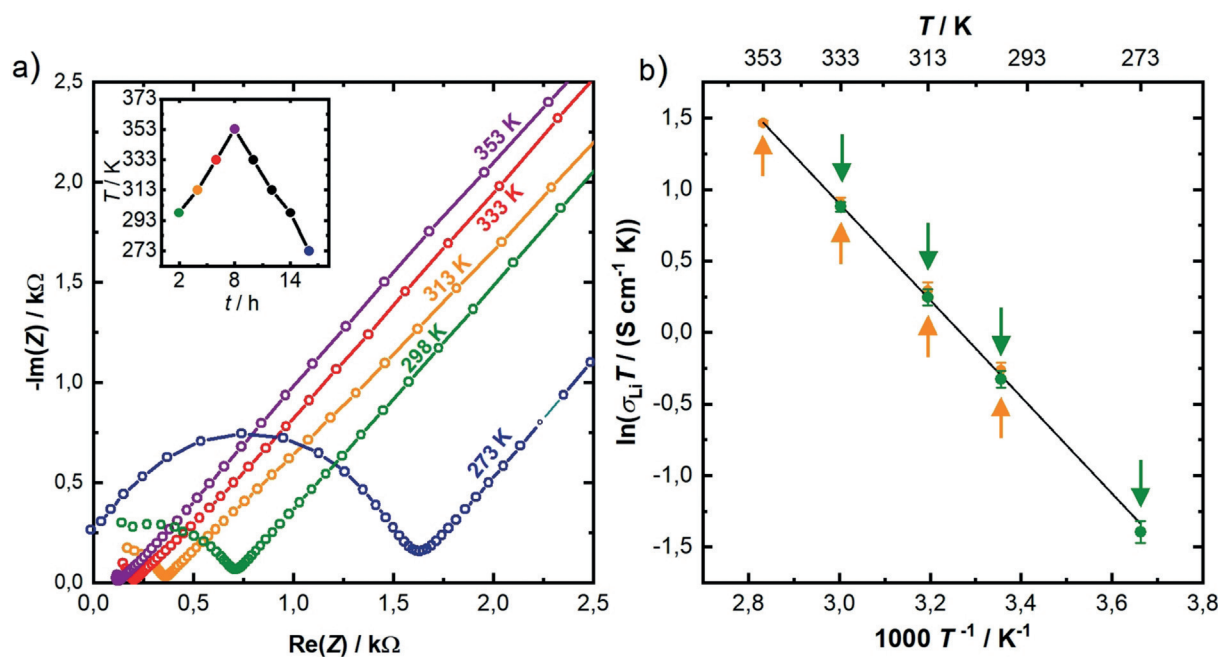


**Figure 4.** a) Nyquist plot of  $\text{Li}_9\text{AlP}_4$  measured under blocking conditions, with spectra recorded at temperatures between 273 and 353 K during a heating cycle, acquired in a sequence described by the color-coded points marked in the temperature profile that is shown in the inset (note that the 273 K data were acquired at the end of the first heating and cooling cycle). b) Arrhenius plot of the product of conductivity and temperature ( $\sigma_{\text{Li}} T$ ) obtained in the heating (orange) as well as in the cooling (green) branch, with error bars for each based on the standard deviation from independent measurements with three cells; the shown linear fit through both branches was used to obtain the activation energy  $E_{\text{A}}^{\text{PEIS}}$ . Since the differences of the average ( $\sigma_{\text{Li}} T$ ) values obtained during heating vs. cooling are very small; they are marked by the orange and green arrows, respectively.

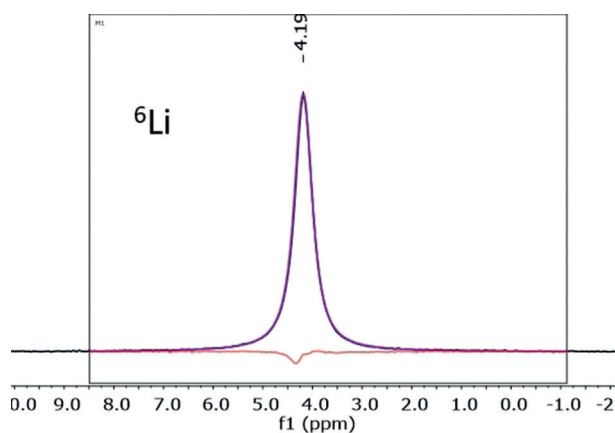


**Figure 5.**  $^6\text{Li}$  MAS NMR measurement of  $\text{Li}_9\text{AlP}_4$ . The inset shows the region of data fitting. The black, pink, and red lines indicate the experimental and calculated signal and the difference line, respectively. Full width at half maximum is 19.2 Hz.

content, tetrahedral voids are slightly less occupied, whereas in the octahedral voids more lithium is found in  $\text{Li}_9\text{AlP}_4$  compared to the situation in  $\beta\text{-Li}_8\text{GeP}_4$ : in  $\text{Li}_9\text{AlP}_4$  90% of the tetrahedral and 58% of the octahedral voids are occupied compared to 93% and 38%, respectively, in  $\beta\text{-Li}_8\text{GeP}_4$ . At a higher lithium content, the lithium ions are more evenly distributed over the tetrahedral and octahedral voids which might mainly result from a lower average electrostatic repulsion. The here observed decrease of lithium content in

the tetrahedral and the increase of lithium content in the octahedral voids in the presence of more lithium is in accordance with the observation made by aliovalent substitution in garnets and was well investigated by Cussen.<sup>[62]</sup> Moreover, this increased population of octahedral voids contributes likely to the energy landscape flattening, as also seen in further electrolytes like in  $\text{Li}_7\text{La}_3\text{Zr}_2\text{O}_{12}$  and argyrodites.<sup>[58,63]</sup> We found that the displacement of the  $\text{Li}^+$  position from the center of the octahedral voids increases with an increasing lithium content per formula unit. And, as also observed in garnets, this stronger displacement correlates with a higher ion mobility. In  $\text{Li}_9\text{AlP}_4$  we found, for the first time in a phosphide-based material, a split position in the octahedral voids. Both positions are close to a triangular plane of the octahedra, supporting the hypothesis of lithium diffusion via face-sharing tetrahedra and octahedra. Lithium migration network analysis in phosphide-based materials like  $\beta\text{-Li}_8\text{GeP}_4$ , has already suggested that lithium diffusion is favored via face-sharing tetrahedra and octahedra.<sup>[48]</sup> Interestingly, the split lithium positions in an octahedral environment, as observed here, has also been found in other fast ion conductors such as sulfide-based electrolytes and garnets: In  $\text{Li}_{10}\text{GeP}_2\text{S}_{12}$  (LGPS), one Li atom (Wyckoff position 8g) exhibits a split position in a slightly distorted  $\text{S}_6$  octahedron,<sup>[59]</sup> and in  $\text{Li}_7\text{La}_3\text{Zr}_2\text{O}_{12}$  (LLZO), one Li atom (Wyckoff position 96h) located in a strongly distorted  $\text{O}_6$  octahedron appears with a split position as well.<sup>[58]</sup>

A change of the metal atom and a higher lithium concentration compared to the previously known compounds

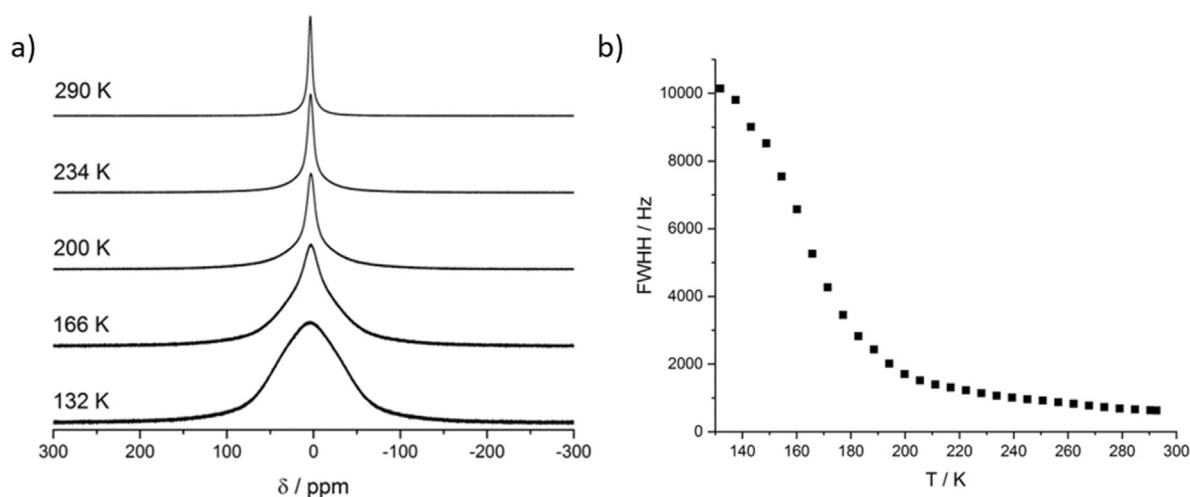


**Figure 6.** a) Temperature-dependent evolution of the  $^7\text{Li}$  lineshape recorded in the temperature range from 132 to 290 K. b) Temperature-dependent linewidth of the  $^7\text{Li}$  signal (full width at half height) recorded in the temperature range from 132 K to room temperature.

**Table 2:** Overview of lithium occupancy, cell volume, lithium ion mobility at room temperature, and Li–P distances in  $\text{Li}_9\text{AlP}_4$ ,  $\beta\text{-Li}_8\text{GeP}_4$ ,  $\alpha\text{-Li}_8\text{GeP}_4$ ,  $\text{Li}_8\text{SiP}_4$ , and  $\text{Li}_{14}\text{SiP}_6$ . Data for the latter four are taken from the literature.<sup>[47–49]</sup>

	$\text{Li}_9\text{AlP}_4$		$\beta\text{-Li}_8\text{GeP}_4$	$\alpha\text{-Li}_8\text{GeP}_4$		$\text{Li}_8\text{SiP}_4$	$\text{Li}_{14}\text{SiP}_6 \equiv \text{Li}_{9.33}\text{Si}_{10.66}\text{P}_4$	
	Wyck.	sof	sof	Wyck.	sof	sof	Wyck.	sof
Tetra-	6b	1	0.78(3)	8c	1	1	8c	0.92(1)
hedral	6c	0.50(5)	1	24d	1	1		
voids	8e	0.71(4)	1	24d	1	1		
	12f	1	1					
	24i	1	0.887(9)					
Octa-	24i	0.46(2)	0.502(9)	4a	1	1	4b	0.50(1)
hedral	24i	0.23(2)	–	24d	–	0.1666		
voids	8e	0.25(4)	–	4b	1	–		
$V [\text{\AA}^3]$		1674.22(2)	1631.75(1)		1643.88(2)	1603.06(2)		209.507(1)
at RT								$\equiv 1676.06(1)$
$\sigma_{\text{Li}}$		$3 \text{ mScm}^{-1}$	$8.6 \times 10^{-5} \text{ Scm}^{-1}$		$1.8 \times 10^{-5} \text{ Scm}^{-1}$	$4.5 \times 10^{-5} \text{ Scm}^{-1}$		$1 \text{ mScm}^{-1}$
at RT								
Li–P		2.50(1)–2.73(1)	2.50(1)–2.69(1)		2.47(2)–2.91(1)	2.51(1)–2.80(1)		2.57(1)
$d_{\text{tet}} [\text{\AA}]$								
Li–P		2.56(1)–3.46(1)	2.82(2)–3.05(2)		2.884(1)–3.028(4)	2.86(1)–3.08(1)		2.97(1)
$d_{\text{oct}} [\text{\AA}]$								

(Table 2) results in an extraordinarily high ionic conductivity of  $3 \text{ mScm}^{-1}$  at room temperature, a very low activation energy of  $29 \text{ kJ mol}^{-1}$  ( $\approx 0.29 \text{ eV}$ ), and a roughly 4 orders of magnitude lower electronic conductivity of  $2.0 \times 10^{-7} \text{ Scm}^{-1}$  at room temperature for the title compound. This high ionic conductivity is achieved by the accommodation of more lithium ions in the octahedral voids. One further benefit of  $\text{Li}_9\text{AlP}_4$  is its very low density of  $\approx 1.7 \text{ g cm}^{-3}$ , which makes the compound very attractive for applications in all-solid-state batteries.

Even though the Li content itself is not a decisive parameter for increasing the Li mobility, the possibility of aliovalent substitution of either  $\text{Li}_{9-x}\text{Tr}_{1-x}\text{P}_4$  ( $\text{Tr}$  = triel element) allows for manifold optimization possibilities. Therefore, we will further investigate the tetrahedral and octahedral occupancy in solid solutions  $\text{Li}_{9-x}\text{Tr}_{1-x}\text{P}_4$ . Further studies will also focus on the thermal behavior and the electrochemical stability of this material. For  $\text{Li}_9\text{AlP}_4$ , tem-

perature-dependent powder neutron diffraction measurements in combination with MEM calculations are scheduled to localize the diffusion pathways.

## Acknowledgements

We greatly acknowledge Johannes Landesfeind and Tanja Zünd for the design of the conductivity measurement cell. V.L.D. acknowledges a Leverhulme Early Career Fellowship and support from the Isaac Newton Trust. This work used the ARCHER UK National Supercomputing Service via EPSRC Grant EP/P022596/1. The work was carried out as part of the research project ASSB coordinated by ZAE Bayern. The project is funded by the Bavarian Ministry of Economic Affairs, Regional Development and Energy.



## Conflict of interest

The authors declare no conflict of interest.

**Keywords:** all-solid-state batteries · impedance spectroscopy · lithium · solid electrolytes · solid-state structures

**How to cite:** *Angew. Chem. Int. Ed.* **2020**, *59*, 5665–5674  
*Angew. Chem.* **2020**, *132*, 5714–5723

- [1] A. Banerjee, Y. Shilina, B. Ziv, J. M. Ziegelbauer, S. Luski, D. Aurbach, I. C. Halalay, *J. Electrochem. Soc.* **2017**, *164*, A6315–A6323.
- [2] E. J. Berg, C. Villevieille, D. Streich, S. Trabesinger, P. Novák, *J. Electrochem. Soc.* **2015**, *162*, A2468–A2475.
- [3] J. B. Goodenough, Y. Kim, *Chem. Mater.* **2010**, *22*, 587–603.
- [4] K. Turcheniuk, D. Bondarev, V. Singhal, G. Yushin, *Nature* **2018**, *559*, 467–470.
- [5] N. S. Choi, Z. Chen, S. A. Freunberger, X. Ji, Y. K. Sun, K. Amine, G. Yushin, L. F. Nazar, J. Cho, P. G. Bruce, *Angew. Chem. Int. Ed.* **2012**, *51*, 9994–10024; *Angew. Chem.* **2012**, *124*, 10134–10166.
- [6] M. Armand, J. M. Tarascon, *Nature* **2008**, *451*, 652–657.
- [7] V. Etacheri, R. Marom, R. Elazari, G. Salitra, D. Aurbach, *Energy Environ. Sci.* **2011**, *4*, 3243–3262.
- [8] Z. Gao, H. Sun, L. Fu, F. Ye, Y. Zhang, W. Luo, Y. Huang, *Adv. Mater.* **2018**, *30*, 1705702.
- [9] Y. Wang, W. D. Richards, S. P. Ong, L. J. Miara, J. C. Kim, Y. Mo, G. Ceder, *Nat. Mater.* **2015**, *14*, 1026.
- [10] X. Yao, D. Liu, C. Wang, P. Long, G. Peng, Y.-S. Hu, H. Li, L. Chen, X. Xu, *Nano Lett.* **2016**, *16*, 7148–7154.
- [11] Y.-S. Hu, *Nat. Energy* **2016**, *1*, 16042.
- [12] A. L. Robinson, J. Janek, *MRS Bull.* **2014**, *39*, 1046–1047.
- [13] C. Yang, K. Fu, Y. Zhang, E. Hitz, L. Hu, *Adv. Mater.* **2017**, *29*, 1701169.
- [14] W. D. Richards, L. J. Miara, Y. Wang, J. C. Kim, G. Ceder, *Chem. Mater.* **2016**, *28*, 266–273.
- [15] J. Janek, W. G. Zeier, *Nat. Energy* **2016**, *1*, 16141.
- [16] J. C. Bachman, S. Muy, A. Grimaud, H.-H. Chang, N. Pour, S. F. Lux, O. Paschos, F. Maglia, S. Lupart, P. Lamp, L. Giordano, Y. Shao-Horn, *Chem. Rev.* **2016**, *116*, 140–162.
- [17] Y. Meesala, A. Jena, H. Chang, R.-S. Liu, *ACS Energy Lett.* **2017**, *2*, 2734.
- [18] P. Knauth, *Solid State Ionics* **2009**, *180*, 911–916.
- [19] Y. Inaguma, L. Chen, M. Itoh, T. Nakamura, *Solid State Ionics* **1994**, *70*, 196–202.
- [20] Y. Inaguma, C. Liqun, M. Itoh, T. Nakamura, T. Uchida, H. Ikuta, M. Wakihara, *Solid State Commun.* **1993**, *86*, 689–693.
- [21] O. Bohnke, C. Bohnke, J. L. Fourquet, *Solid State Ionics* **1996**, *91*, 21–31.
- [22] S. Stramare, V. Thangadurai, W. Weppner, *Chem. Mater.* **2003**, *15*, 3974–3990.
- [23] P. G. Bruce, A. R. West, *J. Electrochem. Soc.* **1983**, *130*, 662–669.
- [24] A. D. Robertson, A. R. West, A. G. Ritchie, *Solid State Ionics* **1997**, *104*, 1–11.
- [25] H. Y. P. Hong, *Mater. Res. Bull.* **1978**, *13*, 117–124.
- [26] A. R. Rodger, J. Kuwano, A. R. West, *Solid State Ionics* **1985**, *15*, 185–198.
- [27] R. Kanno, T. Hata, Y. Kawamoto, M. Irie, *Solid State Ionics* **2000**, *130*, 97–104.
- [28] R. Kanno, M. Murayama, *J. Electrochem. Soc.* **2001**, *148*, A742–A746.
- [29] M. Murayama, R. Kanno, M. Irie, S. Ito, T. Hata, N. Sonoyama, Y. Kawamoto, *J. Solid State Chem.* **2002**, *168*, 140–148.
- [30] A. Kuhn, R. Eger, J. Nuss, B. V. Lotsch, *Z. Anorg. Allg. Chem.* **2013**, *639*, 1087–1089.
- [31] N. Kamaya, K. Homma, Y. Yamakawa, M. Hirayama, R. Kanno, M. Yonemura, T. Kamiyama, Y. Kato, S. Hama, K. Kawamoto, A. Mitsui, *Nat. Mater.* **2011**, *10*, 682–686.
- [32] P. Zhou, J. Wang, F. Cheng, F. Li, J. Chen, *Chem. Commun.* **2016**, *52*, 6091–6094.
- [33] H. Aono, E. Sugimoto, Y. Sadaoka, N. Imanaka, G.-y. Adachi, *J. Electrochem. Soc.* **1989**, *136*, 590–591.
- [34] A. Martínez-Juárez, C. Pecharrromán, J. E. Iglesias, J. M. Rojo, *J. Phys. Chem. B* **1998**, *102*, 372–375.
- [35] R. Murugan, V. Thangadurai, W. Weppner, *Angew. Chem. Int. Ed.* **2007**, *46*, 7778–7781; *Angew. Chem.* **2007**, *119*, 7925–7928.
- [36] Y. Li, J.-T. Han, C.-A. Wang, H. Xie, J. B. Goodenough, *J. Mater. Chem.* **2012**, *22*, 15357–15361.
- [37] V. Thangadurai, S. Narayanan, D. Pinzaru, *Chem. Soc. Rev.* **2014**, *43*, 4714–4727.
- [38] H. J. Deiseroth, S. T. Kong, H. Eckert, J. Vannahme, C. Reiner, T. Zaiß, M. Schlosser, *Angew. Chem. Int. Ed.* **2008**, *47*, 755–758; *Angew. Chem.* **2008**, *120*, 767–770.
- [39] M. B. Ley, S. Boulineau, R. Janot, Y. Filinchuk, T. R. Jensen, *J. Phys. Chem. C* **2012**, *116*, 21267–21276.
- [40] T. Lapp, S. Skaarup, A. Hooper, *Solid State Ionics* **1983**, *11*, 97–103.
- [41] H. Yamane, S. Kikkawa, M. Koizumi, *Solid State Ionics* **1987**, *25*, 183–191.
- [42] W. Schnick, J. Lücke, *Solid State Ionics* **1990**, *38*, 271–273.
- [43] M. Matsuo, S. I. Orimo, *Adv. Energy Mater.* **2011**, *1*, 161–172.
- [44] H. D. Lutz, P. Kuske, K. Wussow, *Solid State Ionics* **1988**, *28*–30, 1282–1286.
- [45] Y. Kato, S. Hori, T. Saito, K. Suzuki, M. Hirayama, A. Mitsui, M. Yonemura, H. Iba, R. Kanno, *Nat. Energy* **2016**, *1*, 16030.
- [46] L. Zhou, A. Assoud, Q. Zhang, X. Wu, L. F. Nazar, *J. Am. Chem. Soc.* **2019**, *141*, 19002–19013.
- [47] L. Toffoletti, H. Kirchhain, J. Landesfeind, W. Klein, L. van Wüllen, H. A. Gasteiger, T. F. Fässler, *Chem. Eur. J.* **2016**, *22*, 17635–17645.
- [48] H. Eickhoff, S. Strangmüller, W. Klein, H. Kirchhain, C. Dietrich, W. G. Zeier, L. van Wüllen, T. F. Fässler, *Chem. Mater.* **2018**, *30*, 6440–6448.
- [49] S. Strangmüller, H. Eickhoff, D. Müller, W. Klein, G. Raudaschl-Sieber, H. Kirchhain, C. Sedlmeier, V. Baran, A. Senyshyn, V. L. Deringer, L. van Wüllen, H. A. Gasteiger, T. F. Fässler, *J. Am. Chem. Soc.* **2019**, *141*, 14200–14209.
- [50] A. R. West, *Solid State Chemistry and its Applications*, 2nd ed., Wiley, Chichester, **2014**.
- [51] R. Juza, W. Schulz, *Z. Anorg. Allg. Chem.* **1952**, *269*, 1–12.
- [52] K. Kuriyama, J. Anzawa, K. Kushida, *J. Cryst. Growth* **2008**, *310*, 2298–2300.
- [53] M. Dadsetani, S. Namjoo, *J. Mod. Phys.* **2011**, *02*, 929–933.
- [54] S. R. Yeandel, D. O. Scanlon, P. Goddard, *J. Mater. Chem. A* **2019**, *7*, 3953–3961.
- [55] A. Addamiano, *J. Am. Chem. Soc.* **1960**, *82*, 1537–1540.
- [56] L. Ohse, M. Somer, W. Blase, G. Cordier, *Z. Naturforsch. B* **1993**, *48*, 1027–1034.
- [57] M. Somer, W. Carrillo-Cabrera, K. Peters, H. G. von Schnering, *Z. Kristallogr.* **1998**, *213*, 230.
- [58] Y. Chen, E. Rangasamy, C. Liang, K. An, *Chem. Mater.* **2015**, *27*, 5491–5494.
- [59] D. A. Weber, A. Senyshyn, K. S. Weldert, S. Wenzel, W. Zhang, R. Kaiser, S. Berendts, J. Janek, W. G. Zeier, *Chem. Mater.* **2016**, *28*, 5905–5915.
- [60] H. Eickhoff, L. Toffoletti, W. Klein, G. Raudaschl-Sieber, T. F. Fässler, *Inorg. Chem.* **2017**, *56*, 6688–6694.
- [61] J. S. Waugh, E. I. Fedin, *Sov. Phys. Solid State* **1963**, *4*, 1633.
- [62] E. J. Cussen, *J. Mater. Chem.* **2010**, *20*, 5167–5173.

- [63] S. Ohno, B. Helm, T. Fuchs, G. Dewald, M. A. Kraft, S. P. Culver, A. Senyshyn, W. G. Zeier, *Chem. Mater.* **2019**, *31*, 4936–4944.

Manuscript received: November 15, 2019

Accepted manuscript online: December 11, 2019

Version of record online: January 7, 2020

---